Towards the Modeling of Microgalvanic Corrosion in Aluminum Alloys : the Choice of Boundary Conditions

Nicolas Murer*[1], Nancy Missert[2], Rudy Buchheit[1]
[1]Fontana Corrosion Center, Ohio State University, 2041 College Road, Columbus, OH 43210
[2]Sandia National Laboratories, 1515 Eubank SE, Albuquerque, NM 87123
*Corresponding author: murer.3@osu.edu

Abstract :
Localized corrosion in aluminum alloys is known to occur mostly at the interface of micrometer-sized cathodic intermetallic particles (IMP) and the surrounding matrix via microgalvanic coupling, which brings about local alkalinization.
Nernst-Planck application mode with electroneutrality is used to simulate current and pH distributions resulting from microgalvanic coupling.
Semi-empirical current-potential relations of each metal can be used as boundary conditions. It can alternatively be considered that coupling is controlled by O_2 diffusion-limited cathodic reaction.
To validate which of these boundary conditions gives the most accurate current distribution, a special sample has been designed. It consists of 5 50 µm Cu islands deposited onto 150 µm Al microelectrodes. Current densities are monitored for each Al/Cu system.
The comparison of these current densities with the simulated ones shows that O_2 diffusion control of the coupling is the most realistic boundary condition.
This condition is applied on a 10 µm sized IMP surrounded by anodic matrix to assess the role of alkalinization on the matrix corrosion.

Keywords: Nernst – Planck, galvanic coupling, localized corrosion

1. Introduction

Aluminum alloys in near-neutral, mildly aggressive solutions, undergo damage accumulation during corrosion, mostly due to the presence of micrometer-sized constituent intermetallic particles (IMP) that create a microstructural discontinuity at which localized corrosion occurs. Most of the IMP are known to have a cathodic behaviour relative to the surrounding matrix. The corrosion of the matrix, initiated at the interface, can occur via the destabilization of the passive oxide film. This destabilization has been attributed to a local alkalinization caused by O_2 reduction on the IMP[1,2].
The driving force for localized corrosion has been shown to be a microgalvanic coupling between the cathodic particle and the surrounding anodic matrix[3,4].
The first step in the development of a predictive model for damage accumulation, is the validation of a model that simulates potential and current distributions in a microgalvanic coupling configuration.
Due to the passive nature of aluminum and aluminum alloys and the density and size (around 10 µm) of IMP in real alloys, it is very difficult to record current densities originating from a galvanic coupling between an IMP and the surrounding matrix contained in a real alloys. However, local pH measurements were performed by a microprobe over a synthetic intermetallic phase coupled to a real alloy[1,5]. These measurements were in good agreement with a finite element model based on the assumption of a coupling controlled by O_2 diffusion at the cathode[5]. Another method consisted of measuring the dissolution profile of the anode of a millimetric bimetallic system after corrosion[6]. In this cell, the flow of the electrolyte was controlled ensuring that the coupling was in a steady-state. The dissolution profile was in good agreement with a boundary element model. The boundary conditions were the Butler-Volmer relations fitted on the experimental polarization curves of the two constitutive electrodes of the bimetallic system.
In these two examples, we can see that two types of conditions (current potential relations fitted to experimental curves versus mass transport) can be set at the active boundaries (i.e. the anode and the cathode) depending on whether we consider that the coupling, in a stationary regime, is electron transfer or mass transport controlled.
By confronting the simulated currents with experimental current densities, we can discriminate which boundary conditions are the most appropriate. As said above, it is technically

impossible to record coupling current densities from a single 10 µm IMP/matrix system.
A special sample that allows current densities measurements at a higher scale, but still in the micrometer range, has been designed
It consists of an array of 50 µm Cu islands deposited on 150 µm aluminum microelectrodes. The sample is designed to reproduce the behavior of primary cathodic IMP in a real alloy. Currents can be recorded for each Al/Cu system.
These currents can be compared to the current density distributions obtained by modeling for each of the boundary conditions
The boundary conditions for which the simulated current density distribution is matching the experimental measurements can then be applied to a more realistic geometry i.e. a 10 µm cathodic IMP surrounded by an anodic matrix. The pH evolution can also be described and its effect on the damage accumulation can also be predicted.

2. Experimental

The bimetallic system that is providing experimental data is based on earlier works done on a system composed of arrays of engineered copper islands on an aluminum thin-film matrix[7]. The present system is composed of engineered copper islands also deposited on Al matrix. But each of the copper island is deposited on a separate Al electrode so that the coupling current on each copper island/Al matrix system can be separately recorded. The whole system is composed of 5 channels (Cf. Fig. 1). The gap between each channel is 50 µm and each Al square, on which a Cu island is deposited, is 150 µm. The Cu islands have a diameter of 50 µm.
For each channel the net current is monitored during around 10 min under free corrosion in open-air 10 mM NaCl solution. It appears during the experiment that the net current monitored for channel 1 is anodic and that the other four net currents are cathodic. Coupling occurs not only between Cu and Al on a single channel but also between each channel. The electrolyte thickness is 3.2 mm. This behavior allows us to simplify the geometry (Cf. Fig. 2) that will be used to mimic this polybimetallic system.

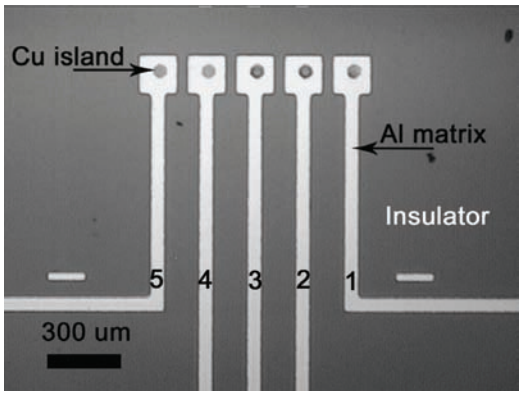

Figure 1 : Optical micrography of the model polybimetallic system, reproducing the behavior of cathodic particles in a real alloy. Coupling occurs between each Cu particle/Al matrix system, in which the Cu particle is cathodic relatively to the anodic Al matrix, but also between each channels.

3. Modeling

3.1 Geometry

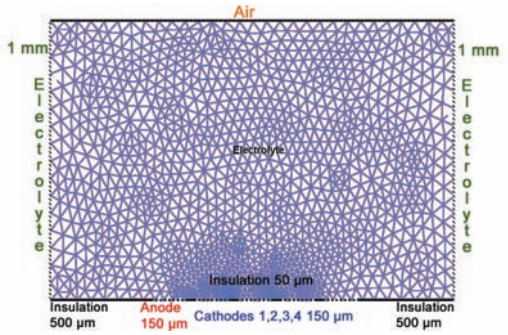

Figure 2 : Geometry used to mimic the system in Fig. 1. Each electrode is separated from each other by a 50 µm insulative gap. Anode corresponds to channel 5 and the cathodes correspond to channels 4, 3, 2, 1.

Figure 2 shows the geometry used to mimic the model bimetallic system. Various boundary conditions are applied to each of the boundaries. They will be described in part 3.4. The length of this geometry is 1.95 mm, which is smaller than the experimental total length of the system (Cf. Fig.1). The electrolyte thickness is also smaller than the experimental electrolyte thickness.It was ensured that the shrinkage of the system didn't affect the potential and current distributions.

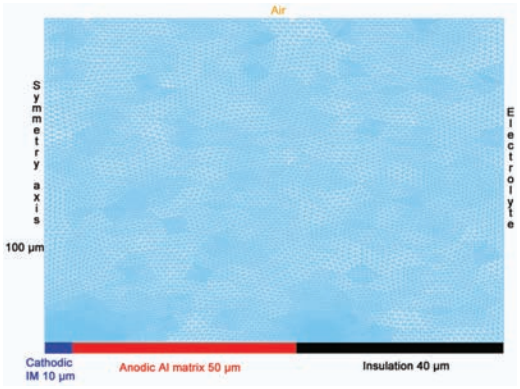

Figure 3 : Geometry of a system comprising a single IMP embedded in an Al matrix. The cathodic IMP, the anodic matrix and the insulation boundary are 10 µm, 40 µm and 50 µm, respectively. The left boundary is a symmetry axis, the height of electrolyte is 100 µm. 10 µm is the average size of the primary IMP found in industrial aluminum alloys.

Figure 3 depicts the more realistic geometry on which the chosen boundary conditions will be applied. It mimics a single 20 µm diameter intermetallic (IM) particle embedded in a 50 µm large matrix ring. The radial symmetry allows us to represent only the radius of the IM.
The thickness of the electrolyte was chosen so that the order of magnitude of each length of the system is similar. In this case, calculations can converge.

For both geometries, we consider the y-axis the axis perpendicular to the electrodes and the x-axis the axis tangential to the electrodes.

Meshing
As it can be seen on Fig. 2 and 3, particular mesh parameters were set at every interface between active boundaries (anodes or cathodes) and another active boundary or insulation boundary. The maximum element size was 1.10^{-6} and the element growth rate was set to 1.3.

3.2 Governing equation

One of the boundary conditions is to consider a cathodically controlled coupling, with the cathodic reaction being limited by O_2 diffusion. In this case, the current distribution is tertiary.
The Nernst-Planck equation with imposed electroneutrality will be used.

Considering that the transport of the considered species does not evolve with time and is controlled only by migration and diffusion, the Nernst-Planck equation, for the species *i*, is[8] :

$$\nabla.N_i = \nabla.(-z_i u_i F c_i \nabla\varphi - D_i \nabla c_i) = R_i \quad (1)$$

Where
N_i is the total flux density of species i ($mol.m^{-2}.s^{-1}$)
φ is the potential in the domain i.e. in the solution (V)
u_i is the mobility of the species i ($m.s^{-1}$)
c_i is the concentration of the species i ($mol.m^{-3}$)
z_i is the charge number of the species i
D_i is the diffusion coefficient of the species i ($m^2.s^{-1}$)
F is the Faraday constant (96500 $C.mol^{-1}$)
R_i is the production term, i.e. the flux of species due to reactions that are occurring in the bulk solution (i.e. subdomain) ($mol.m^{-2}.s^{-1}$). The Nernst-Planck equation is applied to the n species, which gives a *n* equation system with *n+1* variables, the $n+1^{th}$ variable being the potential, The n^{th} variables are the concentrations of the n species. The electroneutrality equation is required to solve this system :

$$\sum_i^n z_i c_i = 0 \quad (2)$$

Current is due to the motion of the charged species :

$$i = F\sum_i z_i N_i \quad (3)$$

3.3 Subdomain conditions

The initial potential of the subdomain was set to V0 = -0.6 V.
6 species were considered as shown in Table 1.
The concentrations are equal to the ones used during the current densities measurements (Cf. part 2). In the subdomain, a reaction term (R in equation 1) for OH^- and H^+ species was used, which is related to the water autoprotolysis :

$$R_{OH^-} = R_{H^+} = k_{wf} - k_{wb}*[OH^-]*[H^+] \quad (4)$$

Where :
k_{wf} is the kinetic forward water dissociation constant in $mol.m^{-3}.s^{-1}$
k_{wb} is the kinetic backward water dissociation constant in $mol^{-1}.m^3.s^{-1}$
$[OH^-]$, $[H^+]$ are OH^- and H^+ concentrations in $mol.m^{-3}$

The ratio k_{wb}/k_{wf} is equal to 1.10^8 and k_{wf} is set to 10^{-4} mol.m^{-3}.s^{-1}.

Table 1: Species, subdomain concentrations and diffusion coefficients.

Species	Initial Concentration (mol.m^{-3})	Diffusion Coefficient (m^2.s^{-1})
Na^+	10	1.10^{-9}
Cl^-	10	1.10^{-9}
OH^-	1.10^{-4}	1.10^{-9}
H^+	1.10^{-4}	1.10^{-9}
Al^{3+}	0	1.10^{-9}
O_2	0.06	1.10^{-9}

1.10^{-4} mol.m^{-3} for OH^- and H^+ concentrations correspond to pH 7.

O_2 concentration was calculated using the relation between the diffusion controlled current on Pt for the reduction of dissolved O_2 and the O_2 concentrations[9].

The conditions of the diffusion controlled current measurement can be obtained on request.

3.4 Boundary conditions

3.4.1 Electrical conditions

For the air and insulation boundaries, the electrical condition was insulation. For the electrolyte boundaries, the initial potential V0 was set. For the active boundaries, the various conditions are described below :

Experimental current densities (EXP conditions)

The net current density was measured for each channel during 10 minutes. To determine the equivalent current density to apply on each electrode we applied the following methodology : we integrated over time the net cathodic currents, and then divided them by the time of the experiment. This way we could reach the average currents for each net cathode. Knowing the surface area of each net cathode (that is to say the copper island on the Al microelectrode), we could determine the average current density.

The current density set at the anode was the negative value of the sum of the net cathodic current densities described above.

Table 2 summarizes the numeric values of the current densities.

Table 2 : Experimental measured current densities

Channel	Type	Average Net Current (nA)	Real Surface (mm^2)	Average Net Current Density (A.m^{-2})
1	Cathode	-6	0.187	-0.032
2	Cathode	-28.28	0.289	-0.1
3	Cathode	-31.2	0.0975	-0.32
4	Cathode	-75.4	0.289	-0.26
5	Anode			0.712

Experimental current-potential relations (I-E conditions)

Polarizations curves were obtained for each type of the electrodes (Al and Cu). Only the anodic branch of the Al curve and the cathodic branch of the Cu curve were considered.

We used semi-empirical relations to fit the experimental curves.

For the cathode, the curve contains a cathodic diffusional plateau :

$$i_C = \frac{i_{c_C} \exp(E_C - (V_m - V))/\beta_C)}{1 + \frac{(i_{c_C} \exp(E_C - (V_m - V))/\beta_C))}{i_{diff}}} \quad (5)$$

The anodic reaction is in a kinetic regime :

$$i_A = i_{c_A} \exp(E_A - (V_m - V))/\alpha_A) \quad (6)$$

where

i_{cC} and i_{cA} are the cathodic and anodic corrosion current densities (A.m^{-2}), respectively.

β_C is the cathodic modified[1] Tafel coefficient for the cathode (V).

α_A is the anodic modified Tafel coefficient for the anode (V).

E_C and E_A are the corrosion potentials of the cathode and the anode (V), respectively.

V_m is the potential of the metal (V), which is set to 0.

V is the potential in the solution (V).

i_{diff} is the cathodic diffusion limited current density (A.m^{-2}).

These parameters were estimated by fitting the above equations for the experimental curves obtained on Al and Cu in the same 10 mM

[1] Real anodic and cathodic Tafel coefficients are the coefficients α and β in this form of Butler-Volmer relation : $i = i_0[\exp(-\alpha f\eta) - \exp(\beta f\eta)]$ where f=F/(RT) and η is $(V-E_{corr})$[10].

electrolyte as the current measurements (Cf. part 2). These parameters are given in Table 3.

Table 3 : Semi-empiric current density-potential relations parameters. Tafel Coef. Stands for the modified Tafel coefficients α_A and β_C.

Electrode	i_c ($A.m^{-2}$)	E (V/SCE)	Tafel Coef. (V)	i_{diff} ($A.m^{-2}$)
Al (anode)	1.10^{-5}	-0.911	0.045	
Cu (cathode)	-1.10^{-4}	-0.282	0.03	$-2.8.10^{-3}$

O_2 diffusion transport control (D-O_2 conditions)
Under these conditions, the galvanic coupling is controlled by the cathodic reaction. The cathodic reaction kinetic is limited by O_2 diffusion.
The considered reaction on the cathode is the reduction of O_2. The reduction of one mole of O_2 requires 4 moles of electrons (Cf. Eq. 9). Hence, the relationship between the cathodic current density j_c and the diffusion flux of O_2, $J_{diff}O_2$, at the cathode surface is :

$$j_c = -4*F* J_{diff}O_2 \quad (7)$$

where F is the Faraday constant.
The anodic current density is equal to the sum of the current densities integrated over all the cathodes length and then divided by the length of the anode.

3.4.2 Electrochemical conditions

Inactive boundaries
The conditions on the inactive boundaries are summarized in Table 4. The value of O_2 concentration at the air interface was set to 0.26 $mol.m^{-3}$ according to the literature[2].

Active boundaries
On the active boundaries we consider two reactions.
Al oxidation on the anode :

$$Al \rightarrow Al^{3+} + 3e^- \quad (8)$$

O_2 reduction at the cathodes :

$$O_2 + 2H_2O + 4\,e^- \rightarrow 4OH^- \quad (9)$$

Table 5 summarizes the conditions for each species, at the anode and the cathode, depending on the type of considered boundary conditions.
Na^+, Cl^- and H^+ don't take part in the electrode reaction. The insulation condition is set for these ions.

Table 4 : Electrochemical conditions on the inactive boundaries

Boundary	Na^+	Cl^-	H^+	OH^-	Al^{3+}	O_2
Electrolyte	Subdomain Concentrations (Cf. Table 1)					
Air	Insulation					0.26 $mol.m^{-3}$
Insulation (Resin)	Insulation					

Table 5 : Boundary conditions for the reactive species at the active boundaries. j_c and j_a are the cathodic and anodic current densities, respectively, whose expression varies depending on the type of chosen conditions (Cf. 3.4.1). Ins. stands for insulation condition.

Boundary	OH^-	Al^{3+}	O_2
EXP Conditions			
Anode	Ins.	$j_a/(3*F)$	Ins.
Cathodes	$-j_c/(4*F)$	Ins.	j_c/F
I-E Conditions			
Anode	Ins.	$j_a/(3*F)$	Ins.
Cathodes	$-j_c/(4*F)$	Ins.	j_c/F
D-O_2 Conditions			
Anode	Ins.	$-j_a/(3*F)$	Ins.
Cathodes	$4*J_{diff}O_2$	Ins.	$cO_2=0$

4. Results and discussion

4.1 Comparison of the current density profiles at the surface of the electrodes for the various boundary conditions.

Figure 4 shows the different current density profiles (named J_chnp in the software) obtained for the various boundary conditions. The current density profiles are cross-section plots performed at y=0 mm and for $0<x<1.95.10^{-3}$ mm.
J_chnp is the modulus of the current density vector.

$$J\_chnp = \sqrt{(J\_x\_chnp)^2 + (J\_y\_chnp)^2} \quad (10)$$

Where J_x_chnp and J_y_chnp are the x and y components of the current density vector, respectively. We set J_chnp<0 when J_y_chnp<0 so that we can differentiate the anodic from the cathodic current densities.
We can see in Fig. 4 that the current profiles obtained in D-O_2 conditions are much more similar to the experimental current profiles than the current profiles obtained for I-E conditions.

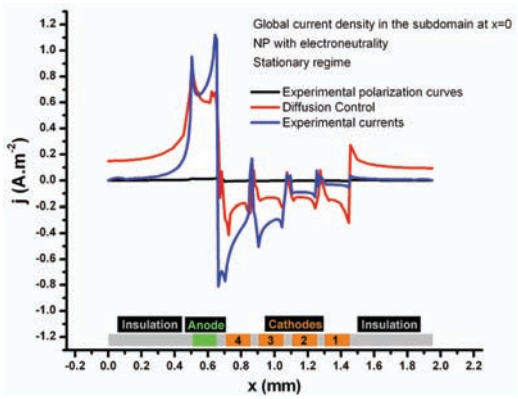

Figure 4 : Current density profiles at the surface of the electrodes for the three different active boundary conditions : semi-experimental i vs E curves (I-E), O_2 diffusion control (D-O_2) and experimental currents (EXP).

For the diffusion control current profiles, current densities at the insulation boundaries are not equal to zero. This comes from the differences in the solving process. For EXP conditions, solving is performed for all the variables whereas for D-O_2 conditions, solving is performed for O_2 only and then for the other variables using the solution formerly obtained.

Table 6 gives the ratio of the surface current densities integrated over the cathodes or anode length, for the various conditions.

We can see in Table 6 that the integrated current densities obtained for I-E conditions are between 80 and 64 times smaller than the experimental integrated current densities whereas the integrated current densities for D-O_2 conditions are almost identical to the EXP conditions integrated currents.

Figure 4 and Table 6 show that the most appropriate boundary conditions to use are the boundary conditions based on an assumption of an O_2 diffusion control.We can now apply these conditions on a system for which the coupling current measurements are not technically possible. This system is depicted by Figure 2 and mimics a real single cathodic IM particle embedded in an anodic matrix.

Table 6 : Comparison of the anodic and cathodic integrated current densities. Current densities are integrated at y=0 for 0.5<x<0.65 mm (anode) and at y=0 for 0.650<x<1.45 mm (cathodes). The ratio of these integrated currents is calculated.
Cf. Fig. 4 for the meaning of the acronyms.

Electrode	EXP/I-E	EXP/D-O_2
Anode	64	1.04
Cathode	80	1.5

4.2 Application of the O_2 diffusion limited boundary condition to a realistic geometry

4.2.1 Conditions

The subdomain conditions are the same as for the Al/Cu geometry, except from the fact that NaCl concentration is set to 1.10^3 $mol.m^{-3}$.

The boundary conditions for the particle are identical to the D-O_2 conditions (Cf. 3.4.1 and 3.4.2). However, following the example of *Alodan and Smyrl*[2], an additional hydrolysis reaction is considered on the anode.

The reaction is the following :

$$Al + 3H_2O \rightarrow Al(OH)_3 + 3H^+ + 3e^- \quad (11)$$

This equation means that an additional inward proton flux proportional to the anodic current density must be taken into account:

$$J_{H+} = j_A/F. \quad (12)$$

We can now describe the pH evolution at the surface of the two electrodes (radial distribution) or in the direction normal to the electrodes plane (vertical distribution) (Cf. Fig. 5).

4.2.2 Radial distribution of pH

According to Fig. 5, an important alkalinization up to pH 9.8 is occurring over the intermetallic particle. It is maintained at 9.8 over the IM particle and drops to bulk pH 6 at almost half the length of the anode. It reaches 4.8 at the end of the anode. Above the resin, the pH increases smoothly to bulk pH.

The pH evolution over the cathode is identical to the ones obtained by *Alodan and Smyrl*[2] and by *Park et al.* [1]. Above the anode, no acidic domain is seen in *Park et al.* works[1] since no hydrolysis reaction was taken into account. For *Alodan and Smyrl*[2], for both profiles the minimum pH is reached just before the matrix/resin interface. This minimum pH is 5.6 in the case of *Alodan and Smyrl*[2] and 4.8 in our case.

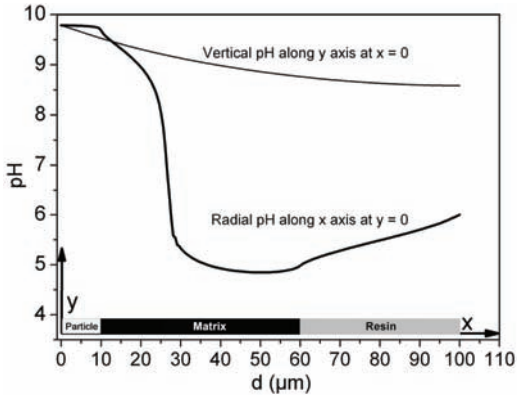

Figure 5 : Simulated radial and vertical pH profiles obtained on the real cathodic IM/anodic 6016 matrix considering an oxygen diffusion limited cathodic reaction.

The difference may be explained by their expression of the H^+ concentration gradient:

$$\frac{\partial cH^+}{\partial y} = \frac{iO_2}{FD_{H^+}} \frac{A_{cathode}}{A_{anode}} \quad (13)$$

With

cH^+ the concentration of H^+ ($mol.m^{-3}$)

y is the vertical coordinate (m)

iO_2 the O_2 diffusion limited cathodic current density ($A..m^{-2}$)

D_{H+} the diffusion coefficient of H^+ ($m^2.s^{-1}$)

$A_{cathode}$ and A_{anode}, the surface of the cathode and the anode, respectively (m^2)

F is the Faraday constant.

The electrode surface ratio being inferior to 1, it explains why the surface pH is higher than in our simulation.

In the model that we used, the radial pH reaches the bulk pH at the far left because the electrolyte boundary condition for H^+ and OH^- was set to the bulk concentration. In Alodan and Smyrl[2] works, the electrolyte boundary condition is insulation, but the length of the resin is high enough (140 µm) to let the pH reach its bulk value.

4.2.3 Vertical distribution of pH

The pH, initially at 9.8, decreases to reach a value close to 9.5 at a height of 100 µm (Fig. 5). In *Alodan and Smyrl*'s works[2], the vertical pH reaches the bulk pH at heights around 100 µm. In our case, the boundary condition at the air interface for H^+ and OH^- species was insulation whereas *Alodan and Smyrl*[2] set bulk concentration condition for the upper boundary. This explains why in their case, the pH reaches the bulk value at 100 µm. By setting insulation condition for every species but O_2 at the upper boundary, we consider that the electrolyte thickness is 100 µm. By setting bulk concentration, *Alodan and Smyrl*[2] consider a semi-infinite electrolyte layer thickness, which may be more realistic.

4.2.4 Using the pH distribution to separate the galvanic and the chemical contributions to the matrix dissolution

The radial distribution of the pH can be used to try to separate the contributions of the pH and of the galvanic coupling to the anodic matrix dissolution.

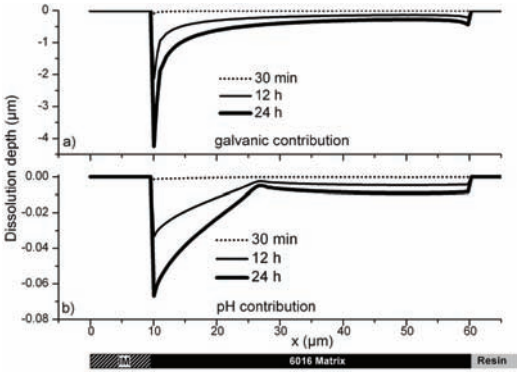

Figure 6 : Calculation of the dissolution depth at the boundary of the IM particle – Al matrix
(a) damage related to the galvanic contribution estimated from Faraday's law applied on the calculated surface current density distribution
(b) damage related to the dissolution estimated by using mass loss versus pH change relation [9] that was then applied to the calculated pH distribution.

In order to have the galvanic contribution, the global current density distribution, obtained by the Nernst-Planck equation resolution, considering a mass transfer control of the coupling, has been converted into dissolution depth by applying Faraday's law for various times (Cf. Fig. 6).

To define the complementary pH contribution, the radial pH distribution on Figure 5 is converted into an anodic dissolution depth profile by using successively a mass loss versus pH curve obtained by *Pryor and Keir*[11] and the Faraday's law.

Pryor and Keir[11] measured the mass loss of Al during 96 hours of exposure in a solution saturated with air for pH ranging from 0 to 14.
Fitting these experimental data with a mathematical equation allows the pH profiles to be converted into a mass loss profile and then, by using Faraday's law, into a dissolution depth profile, again, for various times.
Figure 6 shows that the dissolution depth related to pH is about 200 times less important than the galvanic contribution. Indeed, the dissolution depth obtained with the calculated current is equal, after 24 h, to around 4 µm, whereas for the same time the pH contribution is about 0.07 µm. This result, which has not been experimentally validated, minimizes the role of alkalinization in localized corrosion processes at a cathodic IM/anodic matrix interface.

5. Conclusions

Assuming a control of the cathodic reaction by O_2 diffusion has been shown to provide a simulated coupling current density distribution very similar to the experimental distribution measured on an array of Cu islands deposited on Al matrix.
Using cathodic mass transport control as boundary conditions is subsequently preferred to using current-potential semi-empirical relations for the simulation of microgalvanic coupling on a realistic single IMP surrounded by its matrix.
An actual alkalinization has been shown to take place over the cathodic IM, confirming what has been shown in the literature. However, the effect of this alkalinization on the extent of matrix dissolution is much less than has been hypothesized previously.

6. References

1. J. O. Park, C. H. Paik, Y. H. Huang and R. C. Alkire, Influence of Fe-Rich Intermetallic inclusions on pit initiation on aluminum alloys in aerated NaCl, *J. Electrochem. Soc.*, **146**, 517-523, (1999)
2. M. A. Alodan, W. H. Smyrl, Detection of localized corrosion of aluminum alloys using fluorescence microscopy, *J. Electrochem. Soc.*, **145**, 1571-1577 (1998)
3. R. G. Buchheit, R. P. Grant, P. F. Hlava, B. McKenzie and G. L. Zender, Local dissolution phenomena associated with S Phase (Al_2CuMg) particles in aluminum alloy 2024-T3 *J. Electrochem. Soc.*, **144**, 2621-2628 (1997)
4. A. Garner and D. Tromans, Direct observation of intergranular. corrosion in Al4wt%Cu alloy, *Corrosion*, **35**, 55-60 (1979)
5. J. O. Park, C. H. Paik and R. C. Alkire, Scanning microsensors for measurement of local pH distributions at the microscale *J. Electrochem. Soc.*, **143**, L175-L178, (1996)
6. P. Bucaille, R. Oltra and T. Warner, Theoretical and experimental studies of galvanic corrosion between aluminium and Al-4% Cu alloys, *Materials Science Forum*, **242**, 207-212 (1997)
7. N. Missert, J.C. Barbour, R.G. Copeland, J.E. Mikkalson, The localized corrosion of Al at engineered Cu islands, *JOM*, **7,** 34-37, (2001)
8. J.S. Newman, *Electrochemical Systems*, 2nd Edition, Prentice Hall, (1991)
9. M. Sosna, G. Denuault, R. W. Pascal, R. D. Prien, M. Mowlemb, Development of a reliable microelectrode dissolved oxygen sensor, *Sensors And Actuators B*, **123**, 344-351, (2007)
10. A. J. Bard and L. R. Faulkner, *Electrochemical methods : fundamentals and applications*, p100, p168, 2nd edition, Wiley, New York, (2001)
11. M. J. Pryor and D. S. Keir, Galvanic corrosion, II. Effect of pH and dissolved oxygen concentration on the aluminum-steel couple, *J. Electrochem. Soc.*, **105**, 629-636 (1958)

7. Acknowledgments

N. Murer would like to acknowledge the Fontana Corrosion Center and The Ohio State University for the financial support of this project.